Semisupervised multiattribute seismic facies analysis

Jie Qi[1], Tengfei Lin[1], Tao Zhao[1], Fangyu Li[1], and Kurt Marfurt[1]

Abstract

One of the key components of traditional seismic interpretation is to associate or "label" a specific seismic amplitude package of reflectors with an appropriate seismic or geologic facies. The object of seismic clustering algorithms is to use a computer to accelerate this process, allowing one to generate interpreted facies for large 3D volumes. Determining which attributes best quantify a specific amplitude or morphology component seen by the human interpreter is critical to successful clustering. Unfortunately, many patterns, such as coherence images of salt domes, result in a salt-and-pepper classification. Application of 3D Kuwahara median filters smooths the interior attribute response and sharpens the contrast between neighboring facies, thereby preconditioning the attribute volumes for subsequent clustering. In our workflow, the interpreter manually painted n target facies using traditional interpretation techniques, resulting in attribute training data for each facies. Candidate attributes were evaluated by crosscorrelating their histogram for each facies with low correlation implying good facies discrimination, and Kuwahara filtering significantly increased this discrimination. Multiattribute voxels for the n interpreter-painted facies were projected against a generative topographical mapping manifold, resulting in n probability density functions (PDFs). The Bhattacharyya distance between the PDF of each unlabeled voxel to each of n facies PDFs resulted in a probability volume of each user-defined facies. We have determined the effectiveness of this workflow to a large 3D seismic volume acquired offshore Louisiana, USA.

Introduction

Seismic stratigraphy plays a key role in the interpretation of many Gulf of Mexico (GOM) seismic surveys. Although many geologic features are represented by a specific geometric pattern, such as channel incisement, angular unconformities against erosional surfaces, and onlap onto smooth horizons, some geologic features are more chaotic and more difficult to describe. Salt domes and mass transport complexes (MTCs) are often seen in offshore data of the GOM. Salt can form seals, whereas MTCs can be seals or drilling hazards. Seismic geomorphology coupled with an appropriate depositional model allows prediction of lithology distribution, deformation features, and overall reservoir heterogeneity. Salt holds an additional interest in the processing shop, in which the accurate definition of high-velocity salt is critical to prestack depth migration. Defining the limits of salt domes in offshore seismic data consumes hours of interpreter time. MTCs often exhibit similar textures to salt in 3D coherence volumes. Both features are difficult to autopick, whereas geobody tools often perform poorly.

The published literature on salt segmentation exceeds that of any other computer-aided facies identification workflow and can be divided into two methods. The first method is based on image segmentation. Lomask et al. (2007) apply a modified version of a normalized cuts image segmentation (NCIS) algorithm, which was first introduced to seismic interpretation as atomic meshing of a seismic image (Hale and Emanuel, 2002). The NCIS was adapted from the eigenvector-based method proposed by Shi and Malik (2000), and it provides a globally optimized solution to the problem of seismic salt-boundary picking. Lomask et al.'s (2007) workflow builds a weighting function, which indicates the presence of a boundary between pairs of voxels in the image. In related work, Halpert et al. (2014) modify a pairwise region comparison algorithm, based on the human-interpreted supervision on one or more 2D slices to guide a 3D segmentation process.

The second method is based on the pattern recognition and texture attribute classification. Gao (2003) applies a gray-level co-occurrence matrix (GLCM) to detect a salt dome and find that one GLCM attribute is insufficient to automatically define the salt boundary. Berthelot et al. (2013) combines several GLCM attributes, spectral components, dip, and coherence and uses a supervised Bayesian classification method to delineate the salt. They focus on texture to characterize the change of seismic character between the salt and

[1]University of Oklahoma, ConocoPhillips School of Geology and Geophysics, Norman, Oklahoma, USA. E-mail: jie.qi@ou.edu; tengfei.lin@ou.edu; tao-zhao@ou.edu; fangyu.li@ou.edu; kmarfurt@ou.edu.

Manuscript received by the Editor 30 June 2015; revised manuscript received 8 October 2015; published online 15 February 2016. This paper appears in *Interpretation*, Vol. 4, No. 1 (February 2016); p. SB91–SB106, 19 FIGS.
http://dx.doi.org/10.1190/INT-2015-0098.1.

surrounding geology. Wallet and Pepper (2013) apply mathematical morphology to a single attribute to constrain texture boundaries, thereby reducing the variance of seismic attributes for improved salt delineation.

Three-dimensional computer-assisted seismic facies classification is based on attributes. West et al. (2002), Meldahl et al.(1999), and Corradi et al. (2009) use interpreter-provided seed points or polygons to train neural network classifiers. Coleou et al. (2003), Gao (2007), Matos et al. (2009), and Roy et al.(2013) use 3D self-organizing maps (SOMs) to compute unsupervised facies volumes that are later calibrated with well control and principles of geomorphology. Roy et al. (2014) use GTM to cluster multiattribute data volumes, which is then compared with well control using the Bhattacharyya distance.

Unlike photographic images, seismic textures are 3D and contain many voxels. On vertical slices, seismic facies span the continuum from conformal sands and shales to more complex turbidites, to highly deformed MTCs, and to chaotic salt. To segment such facies, it is necessary to quantify the differences in their seismic attribute expression. Barnes and Laughlin (2002) find that the choice of attributes is critical to effective classification.

Skilled human interpreters have little difficulty in differentiating seismic facies, such as salt and MTCs from each other. Teaching a computer to do the same is more difficult, requiring careful psychological analysis of the human process. How does a human interpreter differentiate these two chaotic textures? How do we quantify different degrees of chaos?

Figure 1 indicates our seismic facies classification workflow. We begin our paper with a summary of candidate attributes that appear to differentiate the seismic facies of interest. Then, we precondition the attribute volumes through Kuwahara filtering, resulting in a smoother facies response and sharper edges. We then introduce a degree of supervision by computing histograms for each candidate attribute for a suite of user-defined facies. Cross-multiplying these histograms quantifies which attributes best differentiate a given facies pair. The selected attributes are then used as input to a GTM classification algorithm. The probability of a given facies at each voxel is estimated using the Bhattacharyya distance. We conclude by validating the predicted facies on seismic vertical lines and time slices that were not used in the training and generating a suite of geobodies.

Attribute expression of seismic facies

Seismic amplitude is the most common attribute used in seismic interpretation. If a geologic feature is not measureable by the spatial variation in the seismic amplitude and phase, no derivative attributes will enable identification. Much of seismic interpretation is based on pattern recognition. Seismic attributes provide quantitative measures of statistical, geometric, or kinematic patterns seen in the 3D seismic amplitude volume. Our initial choice of candidate attributes to differentiate the target seismic facies is based on experience. However, the final choice will be determined through quantitative attribute histogram analysis of manually picked seismic facies.

Figure 2 shows a summary of seismic attribute anomalies associated with different facies seen in the GOM data volume described in this paper. Coherence is sensitive to lateral discontinuities, such as faults, channel edges, and karst (Qi et al., 2014) and chaotic zones, such as salt and MTCs. We use the vector dip

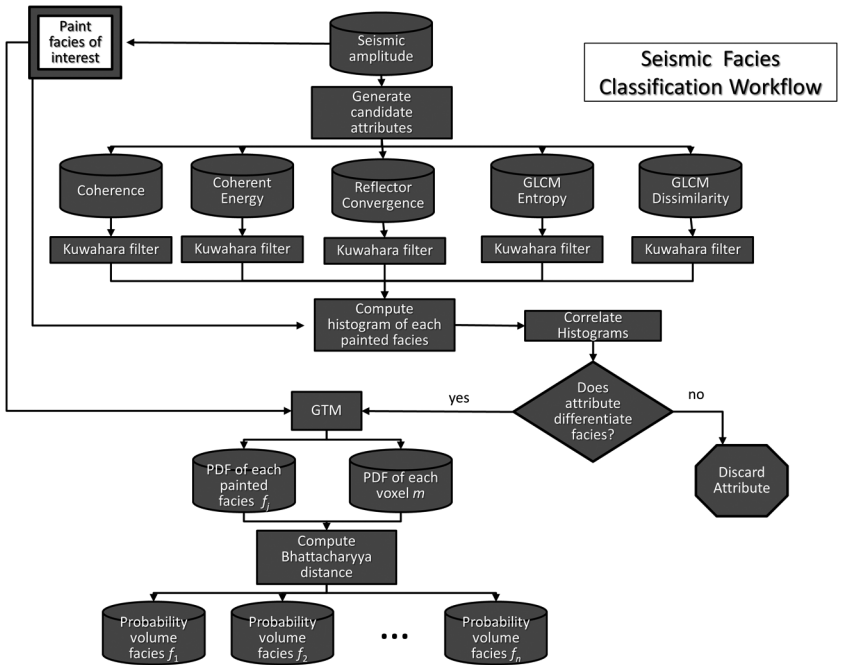

Figure 1. Workflow illustrates the steps used in our multiattribute seismic facies analysis workflow. The interpreter begins by painting target facies of interest on either seismic amplitude or attribute data. After Kuwahara filtering, histograms are computed for each facies and each candidate attribute. Attributes that do not differentiate facies are rejected, whereas those that do are kept and mapped onto a latent space using GTM. Then, the PDF for each facies f is mapped onto the latent space generating a suite of PDFs. Then, the attribute vector at each voxel m is projected onto the latent space, generating an additional PDF. Finally, the probability that a given voxel m belongs to facies f is computed using the Bhattacharyya distance.

as input for principal-component structure-oriented filtering (SOF) in the most coherent window to suppress random and crosscutting coherent noise and improve vertical resolution (Marfurt, 2006). We estimate the coherent part of the data using a Karhunen-Loève filter; the coherent energy is the energy of the Karhunen-Loève filtered data with stronger reflectors exhibiting higher energy than weaker reflectors. Incoherent events internal to salt exhibit the lowest coherent energy. Coherent energy can use to separate a strong reflectivity sand/shale package from a weaker reflectivity shale/shale package.

Although the coherence response to MTCs and salt may be similar, gray-level co-occurrence attributes can

Facies name	Seismic expression	Coherence	Coherent energy	Reflector convergence	GLCM entropy	GLCM dissimilarity
Salt	Low energy, incoherent, vertically and laterally chaotic	"salt and pepper"	Low	Low	High	High
MTC	Mixed energy, incoherent, mixed frequency, piecewise conformal	"salt and pepper"	"salt and pepper"	Low	High	High
Turbidite	Low energy, coherent, piecewise conformal	High	Low	Moderate	Moderate	High
Sand/shale package	High energy, coherent, modern frequency, conformal	High	High	High	Low	Moderate
Shale package	Low energy, coherent, conformal	High	Moderate	High	Low	Moderate

Figure 2. Table of five seismic facies, their seismic expression, and their attribute response seen in this data volume. The recognition of features that allow discrimination between seismic facies is critical. If this can be done, the next most important task is to select attributes that quantitatively measure these features.

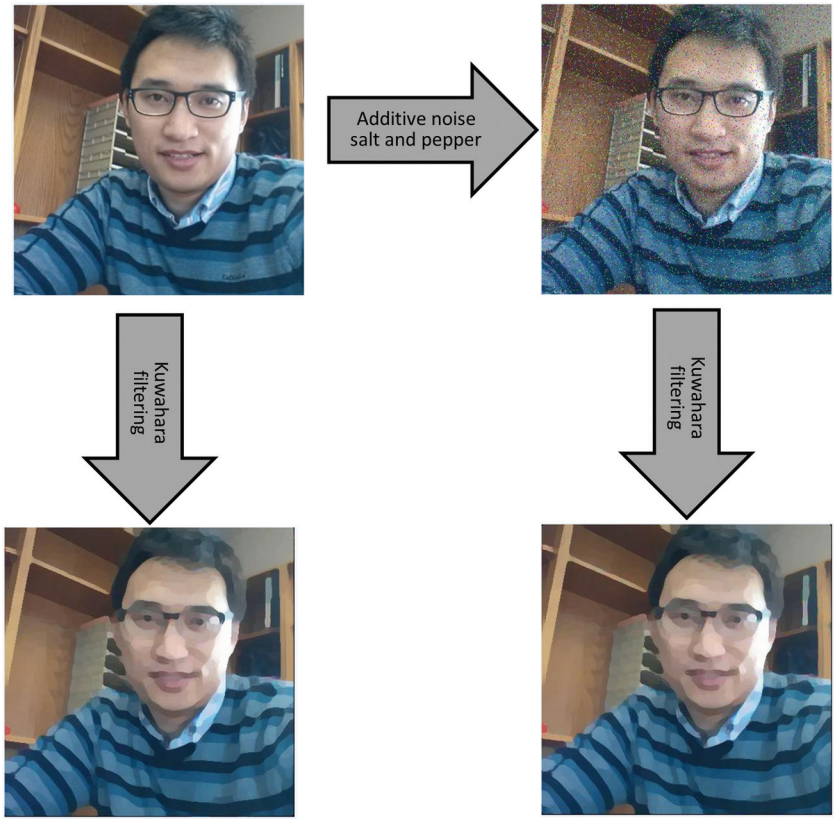

Figure 3. A photo of the first author with and without additive noise before and after Kuwahara filtering applied to each of the R, G, and B components. Note that noise type is salt and pepper. Kuwahara filtering smooths the internal details of the image, but preserves edges.

help to differentiate different kinds of chaotic textures. Texture analysis holds significant promise in computer-aided interpretation and is often used in interpreter-driven or computer-assisted facies analysis (West et al., 2002; Gao, 2007; Corradi et al., 2009). We calculate the GLCM along a structural dip, which quantifies the spatial repeatability (co-occurrence) of voxel amplitude values (gray levels) at a distance within an analysis window. The GLCM entropy is a statistical measure of randomness of the seismic amplitude. The GLCM dissimilarity highlights regions having strict stationary statistics (invariant mean and variance).

The structural curvature is computed by taking the derivatives of the dip components. Reflections that exhibit similar waveforms that, having small offset (<1/4 wavelength) and subtle changes in dip across faults, will generate curvature, but not coherence anomalies (Al-Dossary and Marfurt, 2006). Reflector convergence (Marfurt and Rich, 2010) also differentiates eroded zones from more conformal stratigraphy.

We select five attributes that quantify a specific amplitude or morphology component exhibited by the target. Coherence and reflector convergence can differentiate a chaotic zone, such as a salt dome, or an MTC, from sediment, but not from each of them. Furthermore, local high-coherence zones occur within salt and MTCs given these observation. Texture attributes, such as GLCM entropy and GLCM dissimilarity differentiates chaotic zones, but they are relatively insensitive to seismic facies boundaries. Coherent energy differentiates a strong-reflectivity sand/shale package from a weaker reflectivity shale/shale package, but the MTCs exhibit low- and high-energy elements. Our final task is therefore to precondition the attribute data to provide piecewise smooth images amenable to computer classification algorithms.

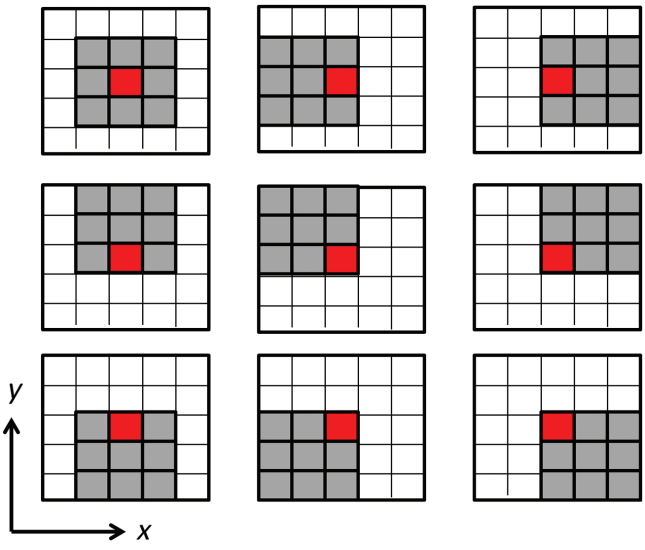

Figure 4. Cartoon of 2D Kuwahara filtering. The input data include 25 samples centered about the red square. The gray squares indicate voxels used in the nine laterally shifted nine-sample analysis windows, each of which contains the output location indicated by the red square. The output is the mean as median of that gray window that has the smallest standard deviation. In 3D, we evaluate 125 neighboring voxels and compute the mean, the median, and standard deviation σ/μ in 27 overlapping $3 \times 3 \times 3$ analysis window.

Kuwahara filtering

Kuwahara et al. (1976) filtering is commonly used in SOF. Kuwahara filters adapt to the variability of the data within overlapping analysis windows, where Luo et al. (2002) use standard deviation followed by a mean filter, and Marfurt (2006) uses 3D coherence followed by a 3D Karhunen-Loève filter to generate edge-preserving SOFs. The Kuwahara filter as an edge-preserving filter is widely used in image processing. Applied to photographs, Kuwahara filters result in piecewise monochromatic features separated by sharp boundaries (Figure 3). By localizing the smoothing, the Kuwahara filter properly removes detail, even salt-and-

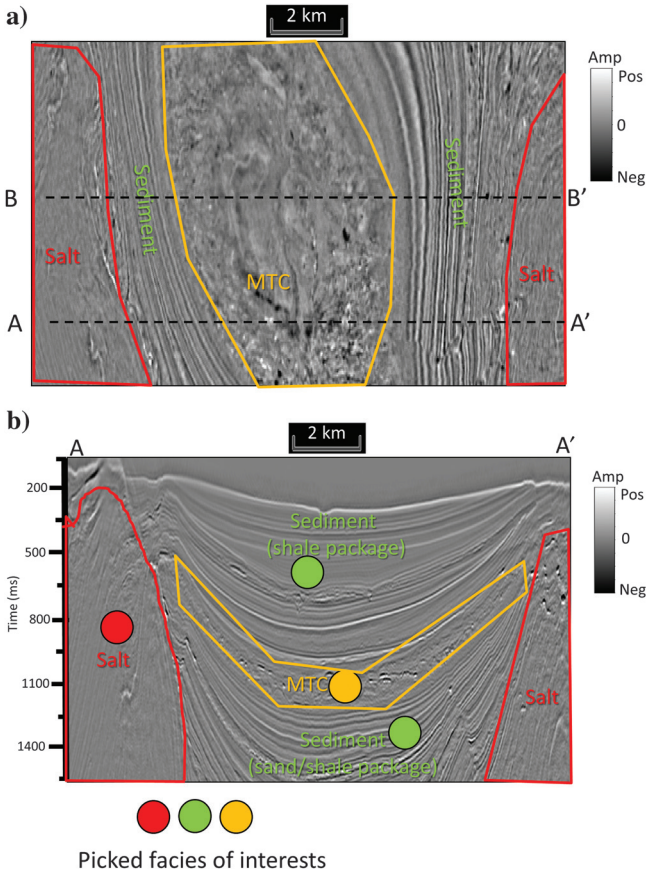

Figure 5. (a) Time slice at $t = 1144$ ms and (b) vertical slice along line AA′ through the seismic amplitude volume. In these images, we have painted two seismic facies of interest: a red salt facies and a yellow MTC facies. Two other facies of interest are a suite of weak reflectors, which we interpret to be shale on shale package, and areas of stronger reflectors that we interpret to be a mixed sand-shale package. Line BB′ has not been interpreted and will be shown in later figures.

pepper noise in high-contrast regions, whereas preserving shape boundaries in low-contrast regions. Kyprianidis et al. (2009) find that the Kuwahara filter "maintains a roughly uniform level of abstraction across the image while providing an overall painting-style look." In our work, we use the same concept to define edges between different types of incoherent zones. Equally importantly, the Kuwahara filter will smooth rapidly varying attribute anomalies within salt and MTCs to facilitate subsequent clustering.

The Kuwahara filter (Figure 4) searches all windows containing a given voxel. In our workflow, the analysis windows are oblique cylinders with radius = 50 m and height of ±20 ms containing $L = 143$ voxels, whose top and bottom faces are aligned with the local dip magnitude and dip azimuth. The L overlapping windows contain any given voxel. For a given attribute, one computes the standard deviation σ, the mean μ, and the median m in each of the L overlapping analysis windows. The filtered attribute will then be the value of m associated with the window having the minimum value of normalized standard deviation σ/μ. The smoothness and noise suppression of an image are controlled by the size of the analysis window. If the analysis window length is large, the image will be smoother, but somewhat blocky. If the analysis window is small, the image will be smoothed less, and blockiness will be reduced. Numerical experiments showed that a single large-window $L = 500$ filter provided superior results to cascading two small-window $L = 143$ filters at reduced computation cost.

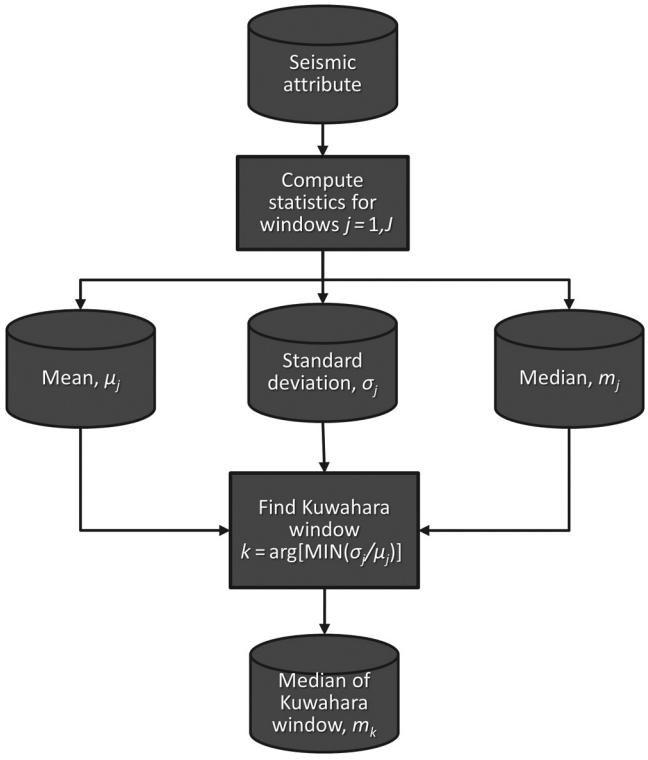

Figure 7. Workflow showing the input to Kuwahara filtering. For each attribute, we first compute the mean, standard deviation, and median for every voxel using a centered J-sample analysis window. Then, find the window k of J non-centered windows containing the target voxel that has the smallest normalized standard deviation σ/μ. Finally, output the median m of window k as the filtered value at the target voxel.

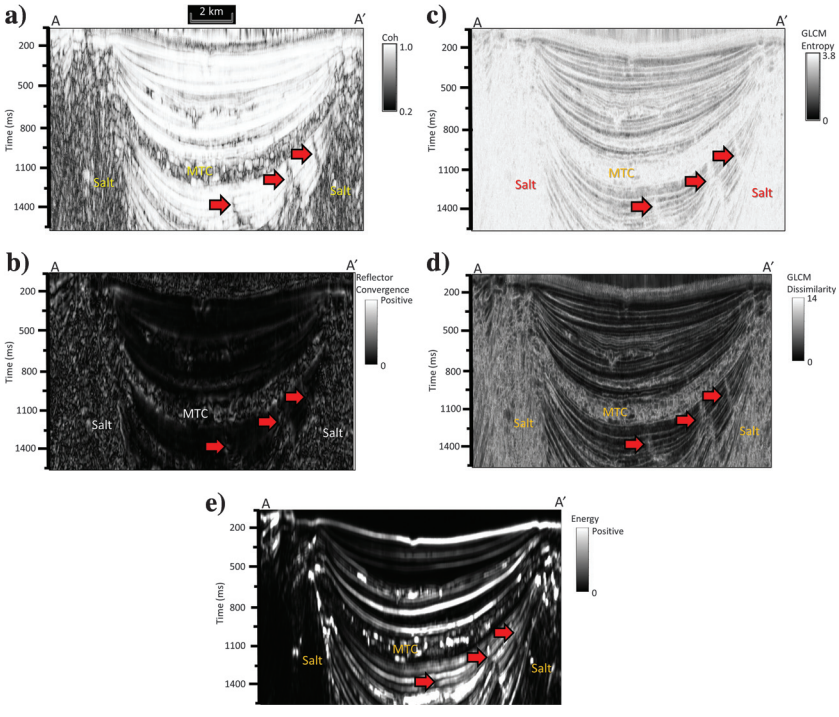

Figure 6. Vertical slices along line AA′ through (a) coherence, (b) magnitude of reflector convergence, (c) GLCM entropy, (d) GLCM dissimilarity, and (e) coherence energy volumes. Note the salt-and-pepper expression of coherence and the magnitude of reflector convergence. The red arrows indicate faults that will either be a separate facies or be misclassified in our attribute-based seismic facies analysis.

Interpreter supervision and attribute histogram analysis

Clustering

The use of classification algorithms to detect natural clusters of attribute responses to geologic facies is referred to as unsupervised classification. In contrast, supervised classification is based on a set of training data, in our case composed of a suite of attribute vectors corresponding to interpreter-picked voxels within a given seismic facies. There are many interpreter-supervised machine-learning methods used in seismic facies classification, such as artificial neural networks, support vectors machines, SOMs, and GTM. SOMs and GTM fit the N-attribute residing in N-dimensional space with a lower dimensional manifold (in our application, a 2D manifold).

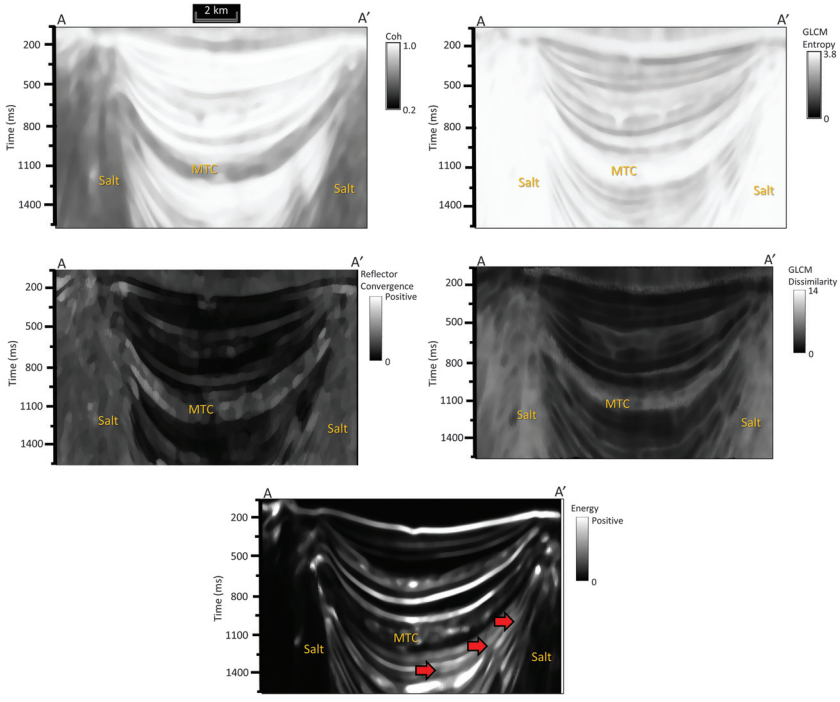

Figure 8. Vertical slices along line AA′ through median-filtered (a) coherence, (b) magnitude of reflector convergence, (c) GLCM entropy, (d) GLCM dissimilarity, and (e) coherent energy. Note that the salt-and-pepper expression of coherence and the magnitude of reflector convergence have been suppressed.

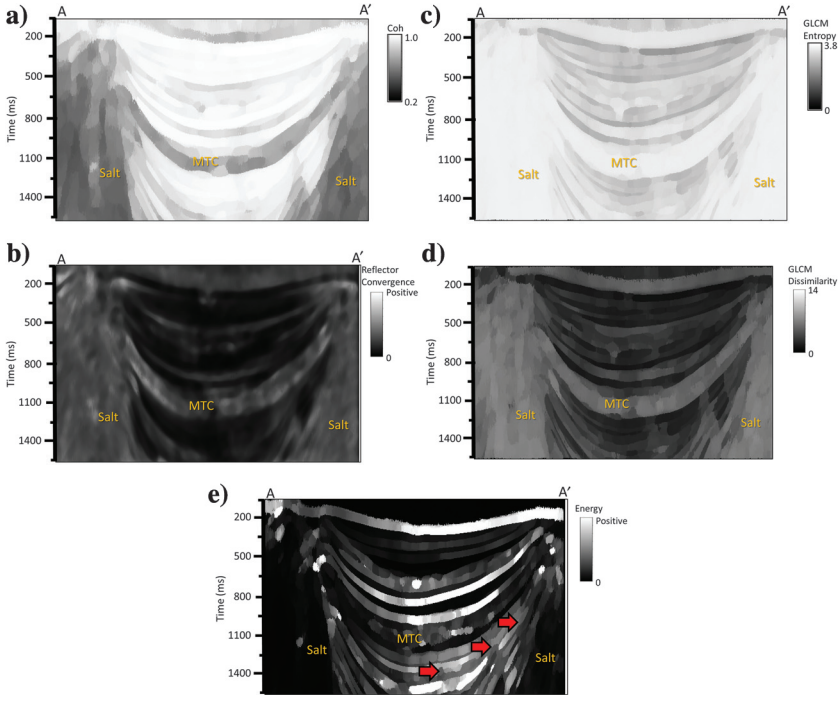

Figure 9. Vertical slices along line AA′ through Kuwahara-filtered (a) coherence, (b) magnitude of reflector convergence, (c) GLCM entropy, (d) GLCM dissimilarity, and (e) coherent energy. Compared with the median-filtered attributes; the Kuwahara-filtered attributes have much clearer edges between any facies.

Attribute histograms

A histogram is a graphical representation of the probability distribution of a quantitative variable. The relationship to geologic events is best understood by examining the data histogram with Sheffield and Parne (2008) finding that effective 3D visualization requires the mapped feature be near a histogram extremum. The correlation coefficient between voxel value histograms of images can be used to detect image content from a large database.

We represent the distribution of attribute values associated with the voxels that fall within an interpreter-painted facies by its histogram. The voxel histogram represents the amplitude distribution of a given attribute, and it represents a probability density function (PDF). A zero-mean seismic amplitude usually has a Gaussian distribution centered around zero. The inclusion of dead traces and mute zones in the histogram calculation results in a spike at value zero and should be avoided. Correlation of histograms is sensitive to their PDF, and it is insensitive to geometric rotation and scaling in seismic data. Luo et al. (2001) introduce a scheme based on histogram equalization to scale seismic data for optimum display. We begin by generating a matrix of histograms for each of the F facies and each of the N candidate attributes. Then for each facies pair (salt versus MTC, MTC versus sediment, or sediment versus salt), we generate a vector of N crosscorrelation coefficients. The histograms from seismic amplitude and seismic attributes contain noise, such that their histograms poorly crosscorrelate. Furthermore, the edges between the different facies may be fuzzy and difficult to identify. Kuwahara filtering of the seismic attributes followed by histogram smoothing addresses these issues. The correlation coefficient r_{fgn} between histogram for

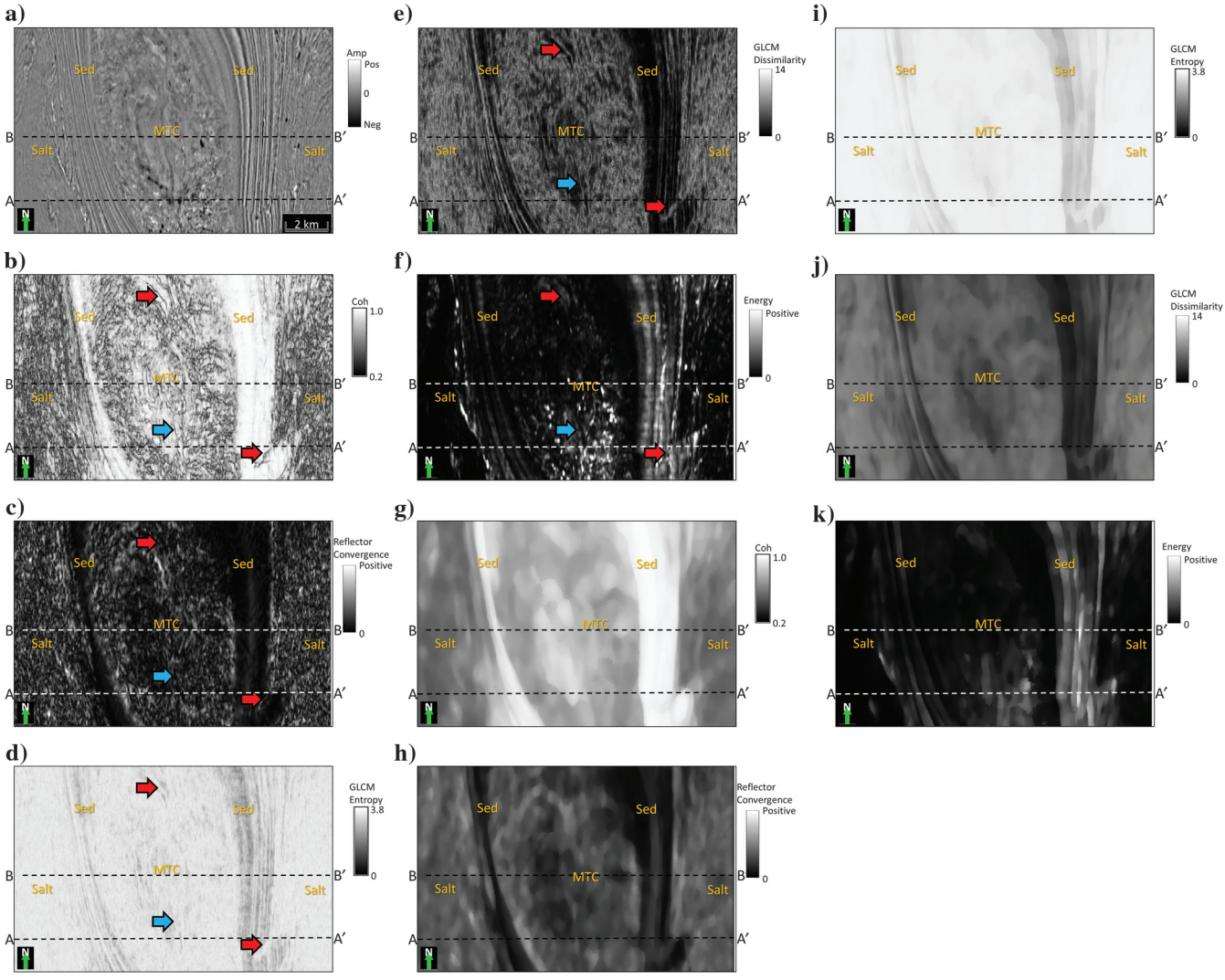

Figure 10. Time slices at $t = 1144$ ms through (a) seismic amplitude, (b) coherence, (c) magnitude of reflector convergence, (d) GLCM entropy, (e) GLCM dissimilarity, and (f) coherent energy. (g–k) Kuwahara-filtered attributes. The Kuwahara-filtered attributes suppress the salt and pepper; these are much clearer boundaries between any two seismic facies. Patterns are easy for human interpreters to identify, but difficult for classifiers to identify as a single face.

facies f h_f and the histogram for facies g h_g for attribute n is

$$r_{fgn} = \frac{\sum_{j=0}^{100}[(h_{fj} - \bar{h}_f)(h_{gj} - \bar{h}_g)]}{\left\{\left[\sum_{j=0}^{100}(h_{fj} - \bar{h}_f)^2\right]\sum_{j=0}^{100}(h_{gj} - \bar{h}_g)^2\right\}^{1/2}}, \quad (1)$$

where the $\bar{h}_f$ and $\bar{h}_g$ are the average of the histogram and where we have constructed our histogram to span 101 bins.

Application

The 3D seismic data cover an area of 8000 km^2 (3089 mi^2) along the current offshore Louisiana shelf edge. The seismic data were acquired by PGS using towed streamer acquisition with two sources and three receiver cables with a maximum offset of 6000 m. We start with a minibasin bound by two salt diapirs to the west and east (Figure 5). The uplift of the western salt dome is contemporaneous with the upper minibasin fill, and it occurred earlier than the eastern salt dome rise.

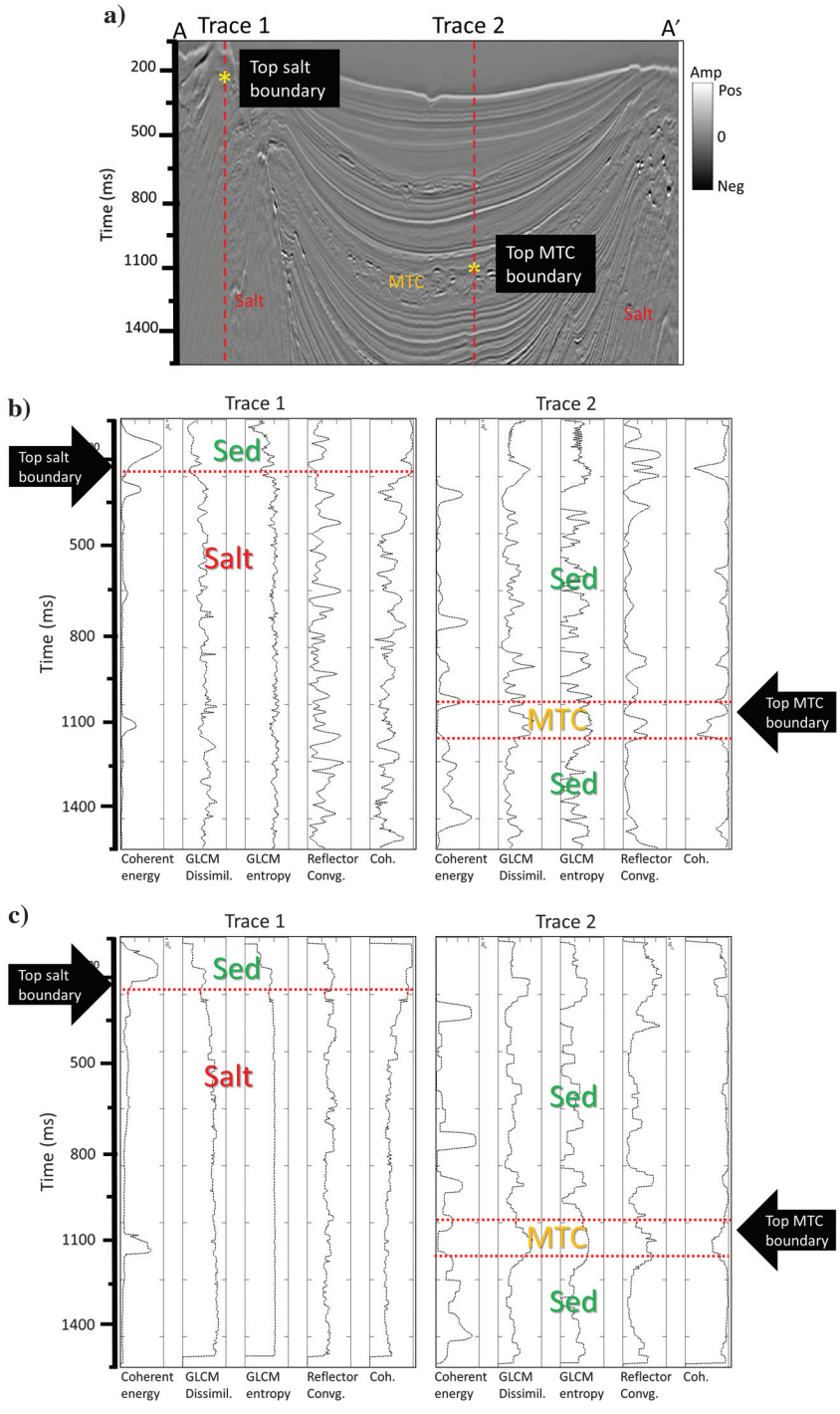

Figure 11. (a) A vertical slice along line AA′ through the seismic amplitude, (b) original attribute values along the trace 1 and the trace 2, and (c) Kuwahara-filtered attribute. Before Kuwahara filtering, values within the salt dome vary rapidly, making it difficult to detect the top salt boundary. In contrast, the Kuwahara-filtered trace shows piecewise smooth values, producing a sharp boundary at the top of the salt dome and MTC.

We interpret (paint) three seismic facies of interest: the salt dome, MTCs, and relatively undeformed sediment that includes strong (an interbedded sand and shale package) reflectors and weak (a thick, predominantly shale package) reflectors. The edge of the salt and the limit of the MTCs can be easily recognized by the human eye. Salt exhibits a lower amplitude and lower frequencies, and it appears to be internally highly chaotic. The MTC exhibits a generally higher amplitude, broadband frequencies, and laterally chaotic and is vertically moderately conformal. The sedimentary packages exhibit alternatively high or low amplitudes, broadband frequencies, are coherent, and are highly conformal.

Although they can be easily recognized by a human interpreter, mapping salt domes and MTCs using voxel-based classifiers is quite difficult. Within the chaotic salt, there may be coherent multiples or coherent migration aliasing artifacts. Within an MTC, there will be a jumble of coherent and incoherent reflectors cut by slump surfaces and small listric and toe-thrust faults.

Seismic attributes

We calculate coherence, coherent energy, magnitude of reflector convergence, GLCM entropy, and GLCM dissimilarity along a structural dip (Figure 6). Examination of Figure 6a shows that the layered sediments exhibit high coherence. Faults, stratigraphic boundaries, and other discontinuities exhibit low coherence. Salt domes have high-coherence inclusions (displayed as white) within a generally low-coherence (black) background, whereas MTCs will have coherent (white), often rotated, reflectors embedded in a relatively incoherent (black) matrix. Thus, in these data, salt and MTC

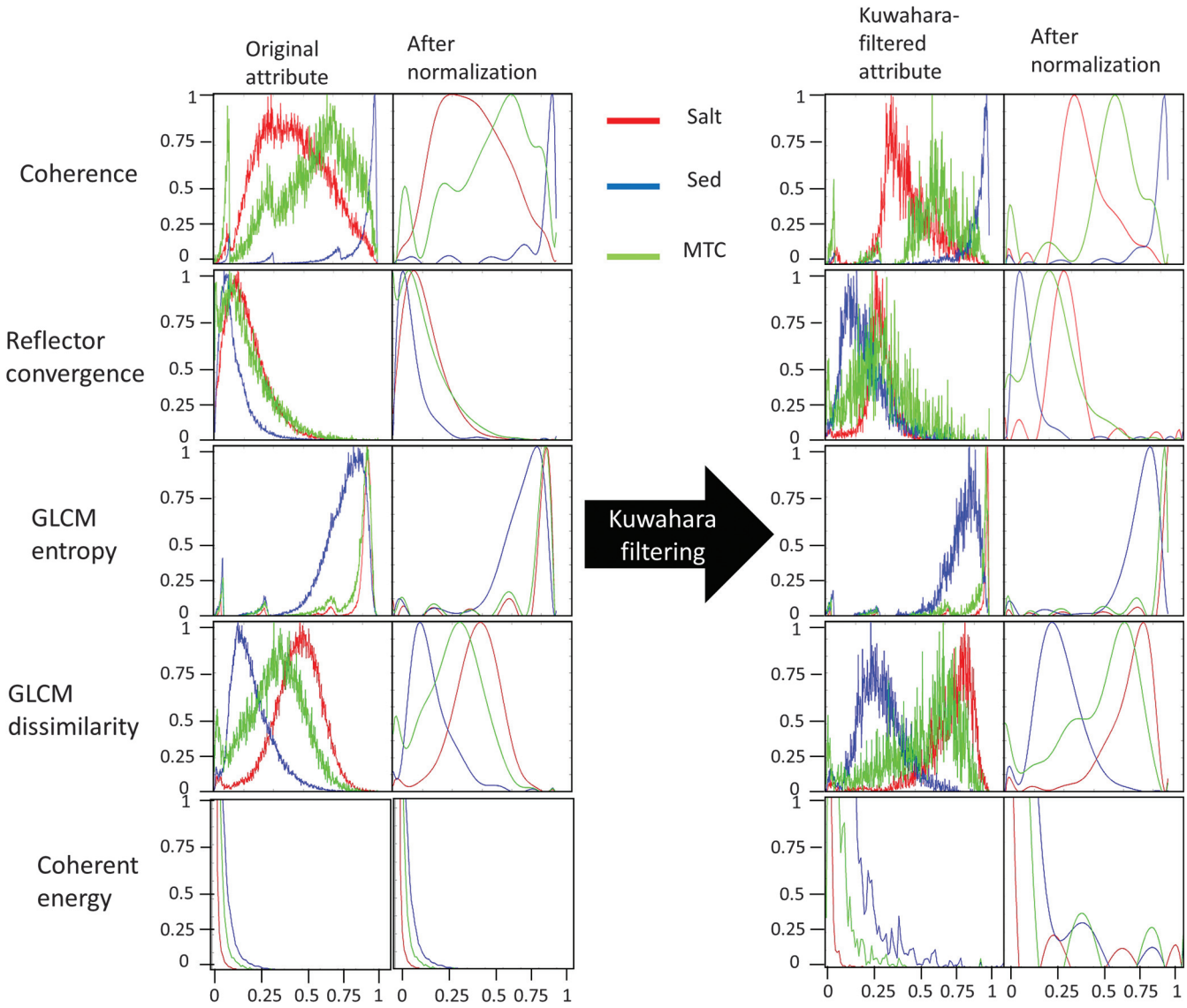

Figure 12. Histograms of picked facies are normalized for easy comparison and do not change the correlation coefficient of any histogram pair. Note that Kuwahara filtering narrows and further separates the distribution of the attribute histograms.

exhibit a salt-and-pepper appearance in coherence volumes. Reflector convergence (Figure 6b) is a 2D vector and shows the magnitude and azimuth of convergence, such as occurs at pinch-outs and angular unconformities. These attributes help to differentiate more fumbled internal salt dome and MTC reflectors from conformably layered stratigraphy. The GLCM entropy (Figure 6c) and GLCM dissimilarity (Figure 6d) show salt domes and MTCs to have high dissimilarity and high entropy, whereas sediments have low entropy and dissimilarity. Coherent energy (Figure 6e) highlights high-reflection coefficient reflectors (the deeper sand/shale package) from low reflectivity, shallower shale/shale packages. Salt appears as low energy with some high-energy inclusions. The MTC is more heterogeneous with high-energy reflectors embedded in a low-energy matrix.

Kuwahara-filtered attributes

Although our preliminary analysis of seismic attributes differentiates the three target facies in this GOM survey, two challenges reduce the accuracy of computer-assisted facies classification. The first challenge is the mixed high- and low-value (salt-and-pepper) anomalies seen in the salt and the MTC. The second challenge is that of additional facies. We have already suggested that the sediments' facies can be broken into a sand/shale versus shale/shale facies. In addition, faults may also be misclassified as one of our three facies. Specifically, the faults in this survey give rise to low coherence, high magnitude of reflector convergence, high GLCM entropy, and high GLCM dissimilarity anomalies. In Figure 6, around the right salt dome, there are three faults (indicated by red arrows) cutting through the salt dome and neighboring sand that exhibit a similar attribute response through the salt and MTC.

We address the first (heterogeneity) problem by applying a Kuwahara filter to smooth rapidly varying attribute anomalies to facilitate subsequent clustering. Figure 7 shows the Kuwahara filtering workflow. One computes three subattributes from each seismic attribute: the standard deviation σ, the mean μ, and the median m in each of the overlapping analysis windows. Figure 8 shows the median m of each candidate attribute, computed within a 100×100 m by ± 12 ms rectangular window, resulting in much smoother, less detailed images. The salt-and-pepper features in the salt and MTC are now more continuous, whereas the thin anomalies associated with the faults are eliminated.

Unfortunately, median filtering has smoothed the edges of seismic facies from rapidly varying to smoothly varying. To apply a Kuwahara filter, we find window k of the L noncentered overlapping windows that contain a target voxel that has the smallest normalized standard deviation σ/μ. Kuwahara filtering then assigns the median of window k to be the output value for the target voxel. In this example, we cascaded two small 50 m radius by ± 8 ms Kuwahara filters. Compared with the median-filtered attributes shown in Figure 8, the Kuwahara-filtered attributes shown in Figure 9 better preserve the boundaries between different seismic facies, preconditioning them for subsequent classification. Figure 10 compares time slices through several attributes before and after Kuwahara filtering, in which we note that the Kuwahara-filtered attributes have smoothed seismic facies (Figure 10). Like the median filter, the Kuwahara filter eliminates thin anomalies, such as faults (red arrows) and channels (blue arrow).

To more clearly see the detailed improvements by Kuwahara filtering, we examine the attributes before and after filtering along two different traces. In Figure 11a, trace 1 intersects a top salt boundary, whereas trace 2 intersects the top and bottom boundaries of MTC. Before filtering (Figure 11b), values within the salt dome vary rapidly, making it difficult to detect the top salt boundary. Likewise, the discrimination of the edges of the MTC is also difficult. In contrast, the Kuwahara-filtered trace in Figure 11c shows piecewise smooth values, producing a sharp boundary of the salt dome and MTC.

a)

Original Attribute	Salt vs. MTC	MTC vs. Sediment	Sediment vs.Salt
Coherence	0.2871	0.1645	0.4526
Reflector convergence	0.8945	0.7385	0.4581
GLCM entropy	0.9336	0.5369	0.3163
GLCM dissimilarity	0.6476	0.3399	0.2612
Coherent energy	0.9546	0.9946	0.9209

b)

Kuwahara-filtered attribute	Salt vs. MTC	MTC vs. Sediment	Sediment vs. Salt
Coherence	0.0434	0.1593	0.2933
Reflector convergence	0.6579	0.2714	0.1363
GLCM entropy	0.6085	0.182	0.0684
GLCM dissimilarity	0.1414	0.1501	0.2435
Coherent energy	0.7362	0.9718	0.6606

Figure 13. Histogram correlation coefficient $r_{fg} < 0.5$ are highlighted in green between (a) original seismic attributes pairs and (b) Kuwahara-filtered attributes pairs.

Attribute selection to separate painted facies

Given these filtered attributes, the next task shown in Figure 1 is to paint the target facies of interest on vertical or time slices and generate histograms for each facies. Figure 12 shows histograms for the three seismic facies: sediment (blue), MTC (green), and salt (red). Histograms of the picked facies are normalized to range between zero and one for easy comparison and do not change the correlation coefficient of any histogram pair. Note that Kuwahara filtering narrows and further separates the distribution of the attribute histograms. Coherence and GLCM dissimilarity attributes now have significantly greater discrimination between the three target facies, allowing the facies to be separated. Reflector convergence and GLCM entropy attributes have poor separation between salt and MTC but good separation of these two facies from the sediments.

Figure 13 compares the correlation coefficients r_{fg} between the original seismic attribute painted facies with those between the Kuwahara-filtered attribute painted facies. For the original attributes (Figure 13a), the histogram correlation coefficients r_{fg} of sediment versus salt are all less than 0.5 for most attributes. In the salt versus MTC facies, only coherence has a low value of r_{fg}, whereas coherence and GLCM-dissimilarity attributes have low values of r_{fg} for the MTC versus the sediment facies. After Kuwahara filtering (Figure 13b), the correlation is significantly reduced, suggesting that our classifier will be better able to discriminate one facies from the other, where the green boxes indicate correlation coefficients of less than a threshold of 0.5. Coupled with the improved edge enhancement of the Kuwahara filter, we expect improved results. Figure 14 shows overlays of the filtered

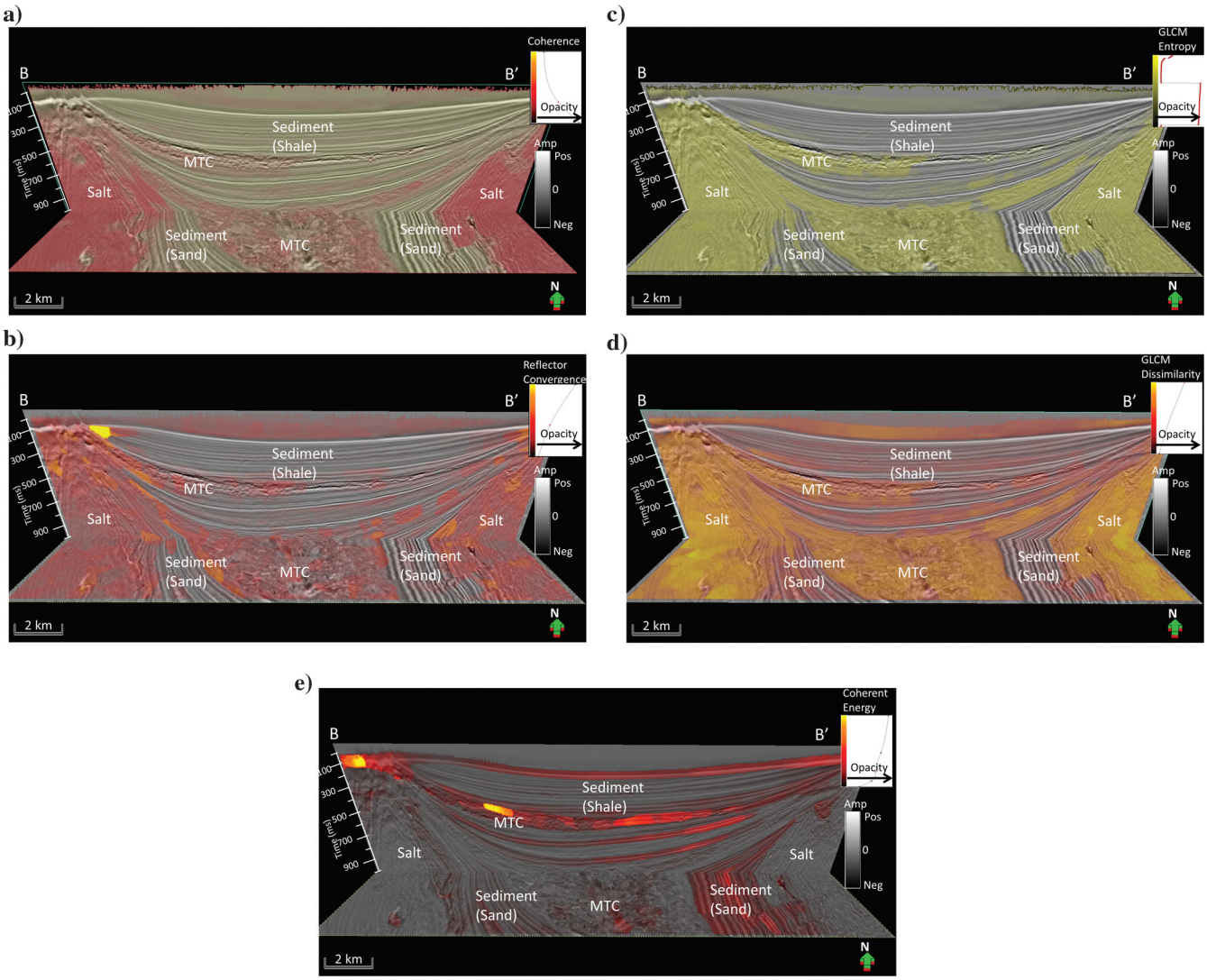

Figure 14. Vertical slices along line BB′ and time slices at $t = 1172$ ms through seismic amplitude corendered with Kuwahara filtered attributes and using threshold attributes (a) coherence, (b) magnitude of reflector convergence, (c) GLCM entropy, (d) GLCM dissimilarity, and (e) coherent energy. Note that the Kuwahara-filtered attributes, with the low facies histogram correlation coefficient (Figure 13b), more clearly block the desired facies. Location of line BB′ is shown in Figure 5.

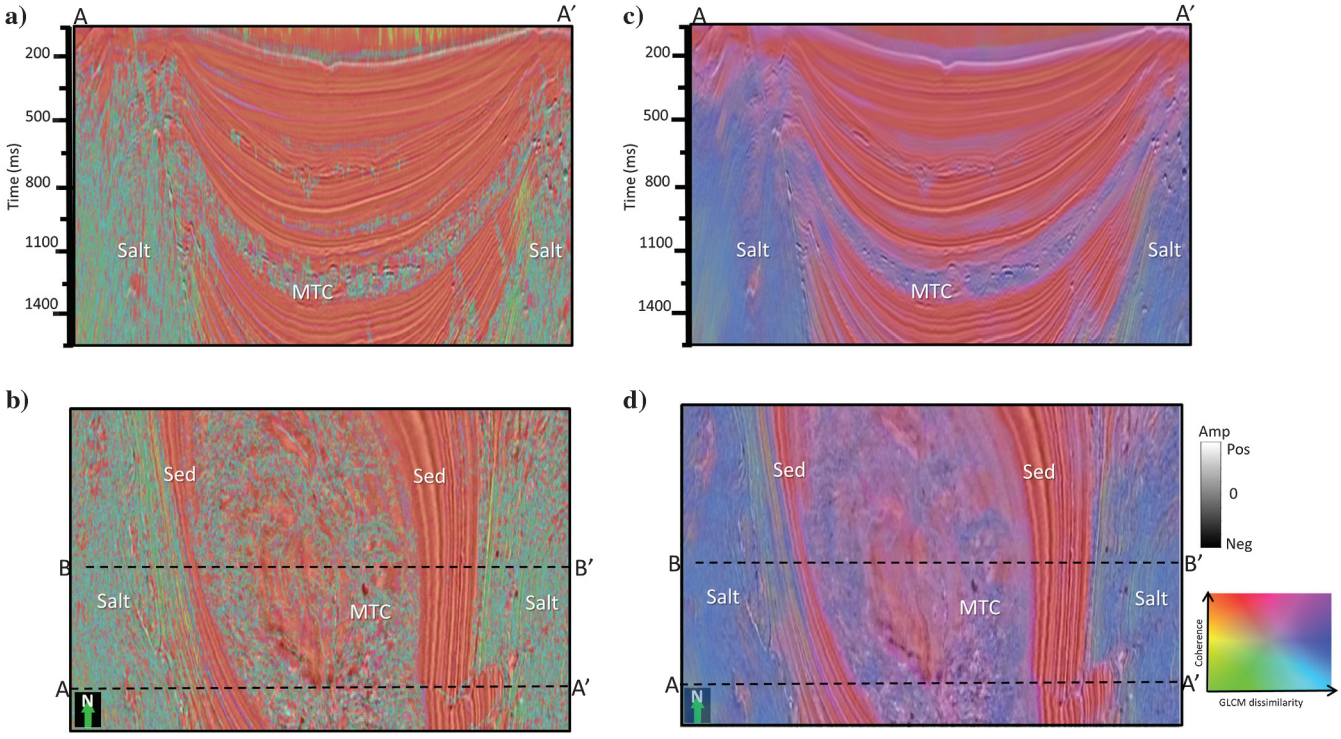

Figure 15. Vertical slices along line AA′ and time slice at $t = 1144$ ms through crossplotted coherence and GLCM dissimilarity before (a) and (b) and after (c) and (d) Kuwahara filtering. Note that the Kuwahara-filtered crossplot shows sharper edges and less internal variation.

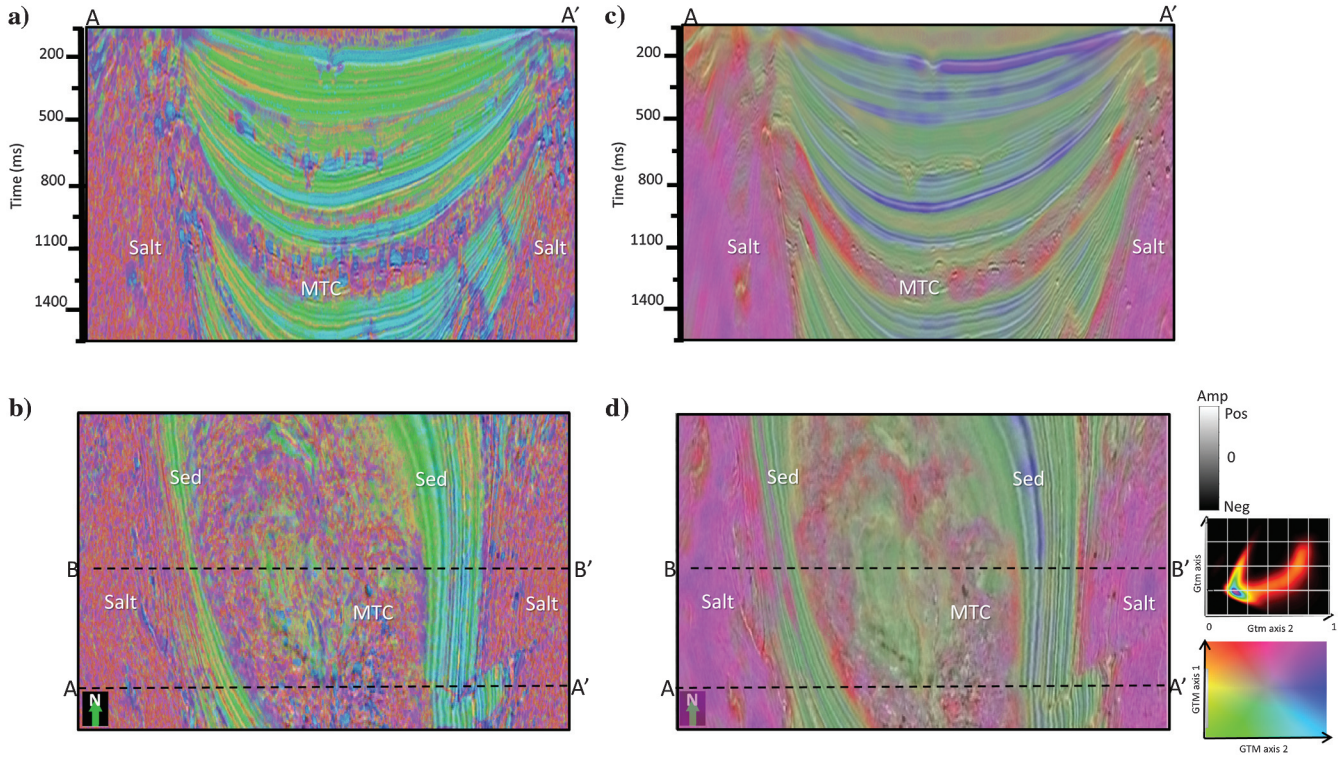

Figure 16. (a) Vertical slices along line AA′ and (b) time slice at $t = 1144$ ms through GTM classification with original attributes use a 2D latent space mapped against; (c) vertical slices along line AA′ and (d) time slice at $t = 1144$ ms through GTM classification with Kuwahara-filtered attributes.

attributes on the vertical seismic slice and time slices at $t = 1172$ ms. Such threshold discrimination between facies is limited to one attribute at a time, although one can sequentially reject larger and larger areas of examination through cascade thresholding of additional attributes.

Crossplotting of two attributes

Crossplotting of seismic attributes is used to highlight relationship of input attributes. In seismic facies analysis, the interpreter picks polygons on the crossplot and display the result, providing a degree of supervision. Figure 15a and 15b shows a vertical section and time slice of original coherence and GLCM-dissimilarity crossplot corendered with seismic amplitude. Figure 15c and 15d shows the same images after by Kuwahara filtering. The crossplotted Kuwahara-filtered images show better facies boundaries and have less internal salt-and-pepper behavior. Unfortunately, crossplotting becomes difficult with three attributes and intractable for more than three facies. Gao (2007) addresses this problem by crossplotting principal components of the attributes, which projects the data onto a plane. Thus, we propose using GTM analysis, which maps data onto a deformed manifold.

GTM interactive clustering and the Bhattacharyya distance

We apply GTM (Roy et al., 2014) to obtain vector projections of multiple attributes onto a 2D latent space. On this example, GTM represent 5D (five-attribute) data by a lower 2D deformed manifold. The GTM starts with an initial 2D plane, defined by the first two eigenvectors of the 5×5 attribute covariance matrix (i.e., principal

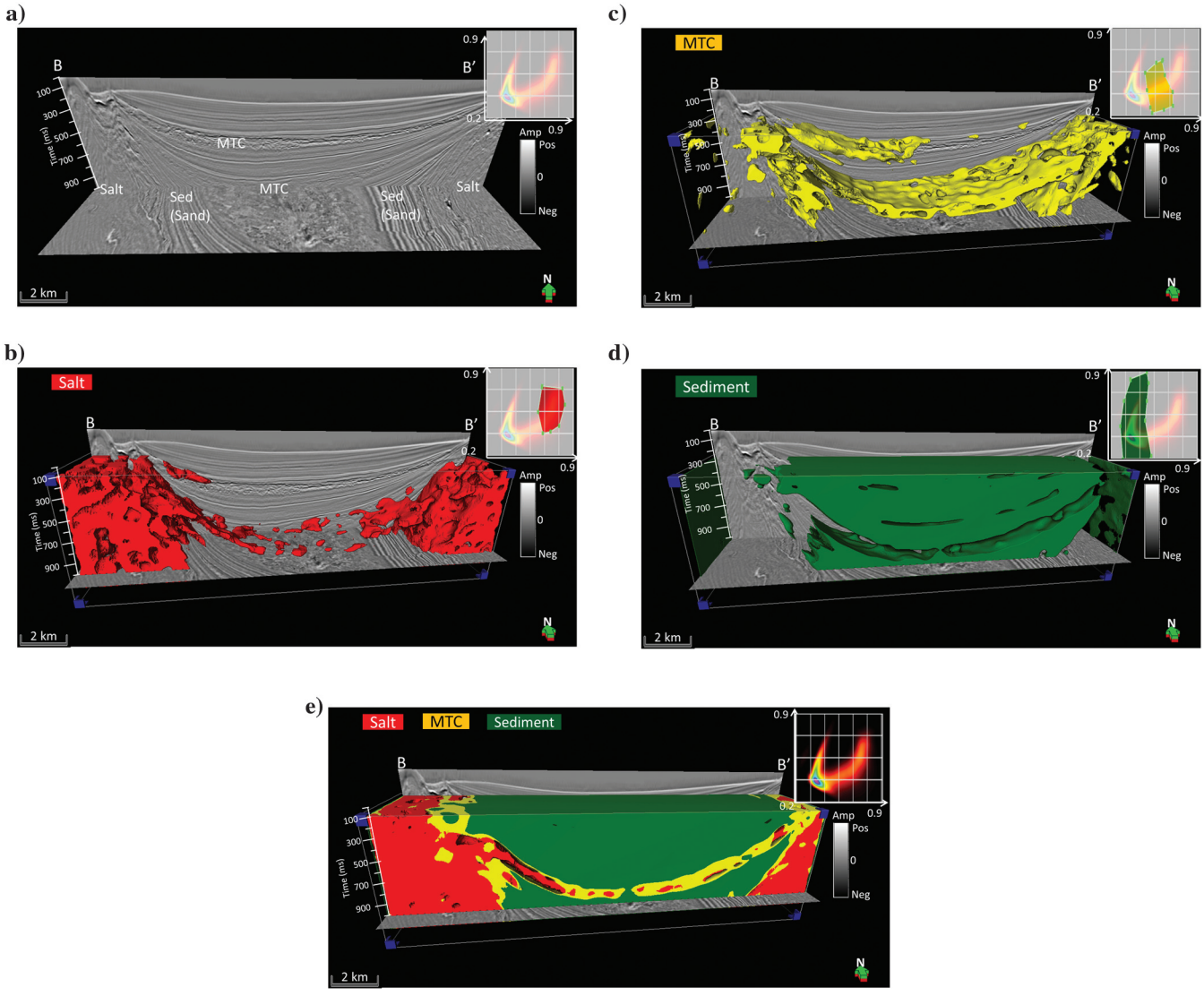

Figure 17. Vertical slices along line BB′ and time slices at $t = 1172$ ms through (a) seismic amplitude and corendered (b) with salt facies (in red), (c) MTC facies (in yellow), (d) sediment facies (in green), and (e) with all three facies obtained by manually drawing a polygon on the GTM histogram.

component analysis). This plane is uniformly populated with clusters, each of which describes a Gaussian PDF. The plane is deformed onto a curved manifold by moving the center of a Gaussian to better fit the data. At each iteration, the variance of the Gaussian is decreased. The process continues until convergence, providing a maximum likelihood estimation of the Gaussian centers. At the end, all vectors are projected onto a 2D latent space.

From our histogram analysis, the five-attribute volumes used in the GTM are coherence, magnitude of reflector convergence, GLCM entropy, GLCM dissimilarity, and coherent energy, representing the depositional features seen in the seismic facies volume. After training, the 5D attribute vectors at each voxel are projected onto the 2D latent space.

Figure 16a and 16b shows the slices through the unsupervised GTM volume computed using the original attribute corendered with seismic amplitude. Figure 16c and 16d shows the slices through the GTM volume computed by Kuwahara-filtered attributes corendered with seismic amplitude. Each voxel is projected onto the 2D latent space that is mapped against a 2D colorbar. Users can then define polygons about hypothesized clusters on display then using commercial crossplotting tools. The salt, MTC, and sediment can be differentiated, where purple indicates salt, red indicates MTCs, green indicates the low-amplitude conformal shale packages, and blue indicates the high-amplitude conformal water bottom and sand/shale packages. Figure 17a shows vertical slice BB′ and time slice at $t = 1172$ ms, through the seismic amplitude. By drawing polygons on the GTM 2D histogram, we define geobodies of salt (Figure 17b), MTCs (Figure 17c), and sediment (Figure 17d). To more quantitatively introduce supervision, we project each painted face onto the previously trained 2D manifold, generating average PDFs for each facies. We then project each 5D data voxel onto the same manifold, generating its own PDF. The Bhattacharyya distance (Roy et al., 2014), which measures the similarity between two PDFs, is then calculated between the voxel PDF with each facies PDF. We first run our method on a few seismic lines. At the paint, the clustering is "unsupervised". We add supervision by projecting the voxels painted in Figure 5b onto the latent space, generating PDFs for salt, MTC, and sediment facies (Figure 18a–18c). To

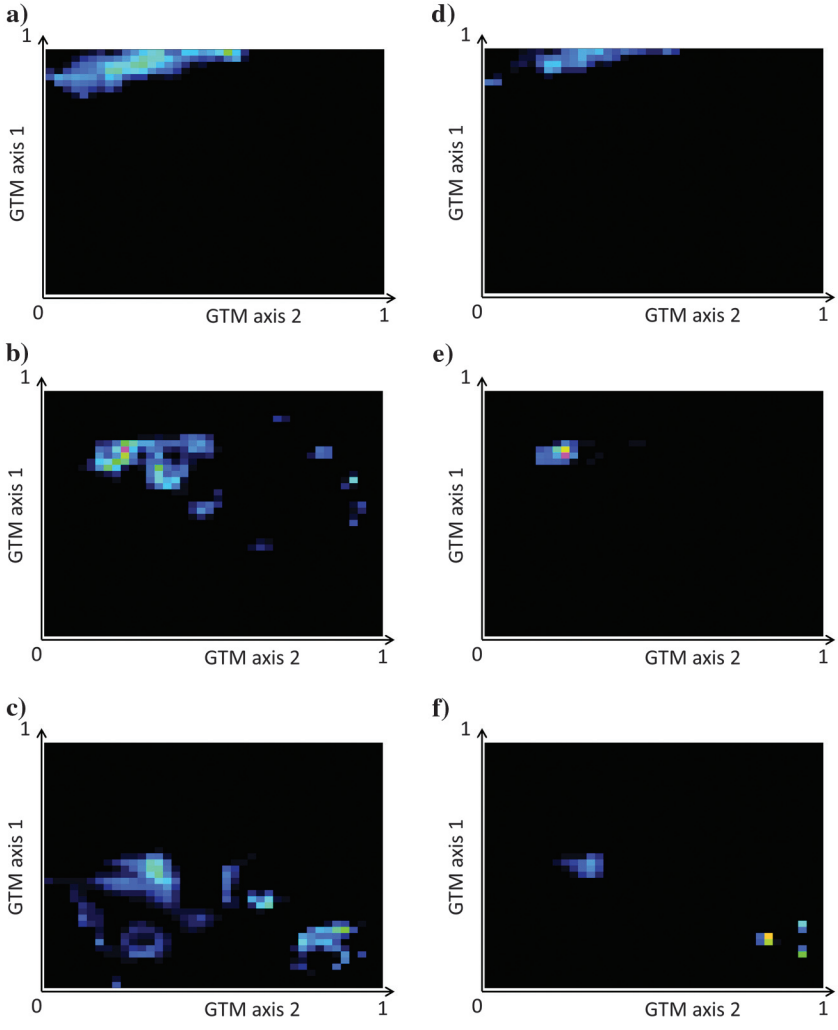

Figure 18. The voxels painted in Figure 5b onto the latent space, generating PDFs for (a) salt, (b) MTC, and (c) sediment, and the single voxels painted in Figure 5b, generating PDFs for (d) salt, (e) MTC, and (f) sediment.

validate these PDFs, we pick single voxels for each facies on a line in a different part of the survey, and we project them on the latent space (Figure 18d–18f). Note that the PDF of the single voxel falls with the PDF of the supervision data. Cross-multiplying the PDF of a given voxel and the PDF of the supervision gives the square of the Bhattacharyya distance. The Bhattacharyya distance determines how likely the voxel belongs to each facies.

Figure 19 shows seismic amplitude corendered with Bhattacharyya-distance volumes for each of the supervised facies. The Bhattacharyya distance provides a probability measurement of how likely a facies is to appear at a certain spatial location. A Bhattacharyya-distance value of 0.8 against salt means that the analysis point is 80% likely to be salt. Such probability estimation is especially useful when there is no clear separation within a transition zone among multiple facies.

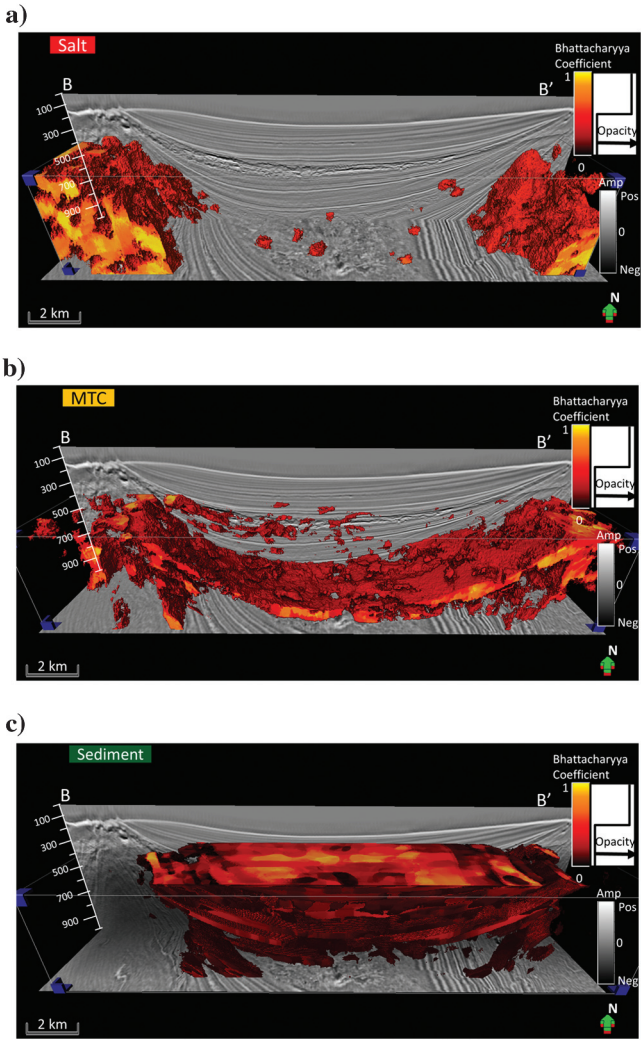

Figure 19. Vertical slice along line BB′ and time slice at $t =$ 1172 ms through seismic amplitude, and corendered with Bhattacharyya coefficient associated with (a) salt, (b) MTC, and (c) sediment facies.

Conclusions

We have developed a workflow to automate the volumetric delineation of seismic facies, with a focus on chaotic facies such as salt diapirs and MTCs common in the GOM. Key to such classification is the choice of attributes that capture patterns seen by the human interpreter that help identify the target facies. Human interpreters see patterns and facies boundaries at scales larger than a few voxels. We approximate this pattern recognition by applying 3D Kuwahara filtering to each attribute volume. The GTM not only allows clustering of the attribute data, but it also facilitates the introduction of interpreter-provided supervision, resulting in a probabilistic volume of each desired facies. The Bhattacharyya distance between the PDF of each unlabeled voxel to each of n facies PDFs results in a probability volume of each user-defined facies.

Acknowledgments

We would like to thank the PGS for providing a license to their data for use in research and education. We also thank the sponsors of the University of Oklahoma Attribute-Assisted Processing and Interpretation Consortium for their guidance and financial support.

References

Al-Dossary, S., and K. J. Marfurt, 2006, 3D volumetric multispectral estimates of reflector curvature and rotation: Geophysics, **71**, no. 5, P41–P51, doi: 10.1190/1.2242449.

Barnes, A. E., and K. J. Laughlin, 2002, Investigation of methods for unsupervised classification of seismic data: 72th Annual International Meeting, SEG, Expanded Abstracts, 2221–2224.

Berthelot, A., A. H. S. Solberg, E. Morisbak, and L. J. Gelius, 2013, Texture attributes for detection of salt: Journal of Applied Geophysics, **88**, 52–69, doi: 10.1016/j.jappgeo.2012.09.006.

Coleou, T., M. Poupon, and K. Azbel, 2003, Unsupervised seismic facies classification: A review and comparison of techniques and implementation: The Leading Edge, **22**, 942–953, doi: 10.1190/1.1623635.

Corradi, A., P. Ruffo, A. Corrao, and C. Visentin, 2009, 3D hydrocarbon migration by percolation technique in an alternative sand-shale environment described by a seismic facies classification volume: Marine and Petroleum Geology, **26**, 495–503, doi: 10.1016/j.marpetgeo.2009.01.002.

Gao, D., 2003, Volume texture extraction for 3D seismic visualization and interpretation: Geophysics, **68**, 1294–1302, doi: 10.1190/1.1598122.

Gao, D., 2007, Application of three-dimensional seismic texture analysis with special reference to deep-marine facies discrimination and interpretation: An example from offshore Angola, West Africa: AAPG Bulletin, **91**, 1665–1683, doi: 10.1306/08020706101.

Hale, D., and J. Emanuel, 2002, Atomic meshes of seismic images: 72nd Annual International Meeting, SEG, Expanded Abstracts, 2126–2129.

Halpert, A. D., R. G. Clapp, and B. Biondi, 2014, Salt delineation via interpreter-guided 3D seismic image segmentation: Interpretation, **2**, T79–T88, doi: 10.1190/INT-2013-0159.1.

Kuwahara, M., K. Hachimura, S. Eiho, and M. Kinoshita, 1976, Digital processing of biomedical images: Plenum Press.

Kyprianidis, J. E., H. Kang, and J. Döllner, 2009, Image and video abstraction by anisotropic Kuwahara filtering: Computer Graphics Forum, **28**, 1955–1963, doi: 10.1111/j.1467-8659.2009.01574.x.

Lomask, J., R. G. Clapp, and B. Biondi, 2007, Application of image segmentation to tracking 3D salt boundaries: Geophysics, **72**, no. 4, P47–P56.

Luo, Y., S. Al-Dossary, and M. Marhoon, 2002, Edge-preserving smoothing and applications: The Leading Edge, **21**, 136–158, doi: 10.1190/1.1452603.

Luo, Y., K. P. Gunaratnam, A. H. Wu, and M. Alfaraj, 2001, Histogram equalization and its application in seismic exploration: 71st Annual International Meeting, SEG, Expanded Abstracts, 1835–1840.

Marfurt, K. J., 2006, Robust estimates of 3D reflector dip and azimuth: Geophysics, **71**, no. 4, P29–P40, doi: 10.1190/1.2213049.

Marfurt, K. J., and J. R. Rich, 2010, Beyond curvature: Volumetric estimates of reflector rotation and convergence: 80th Annual International Meeting, SEG, Expanded Abstracts, 1467–1472.

Matos, M. C., K. J. Marfurt, and P. R. S. Johann, 2009, Seismic color self-organizing maps: Presented at the 11th International Congress of the Brazilian Geophysical Society.

Meldahl, P., R. Heggland, B. Bril, and P. de Groot, 1999, The chimney cube, an example of semi-automated detection of seismic objects by directive attributes and neural networks: Part I — Methodology: 69th Annual International Meeting, SEG, Expanded Abstracts, 931–934.

Qi, J., B. Zhang, H. Zhou, and K. J. Marfurt, 2014, Attribute expression of fault-controlled karst — Fort Worth Basin, TX: Interpretation, **2**, SF91–SF110, doi: 10.1190/INT-2013-0188.1.

Roy, A., B. L. Dowdell, and K. J. Marfurt, 2013, Characterizing a Mississippian tripolitic chert reservoir using 3D unsupervised and supervised multiattribute seismic facies analysis: An example from Osage County, Oklahoma: Interpretation, **1**, SB109–SB124, doi: 10.1190/INT-2013-0023.1.

Roy, A., A. S. Romero-Pelaez, T. J. Kwiatkowski, and K. J. Marfurt, 2014, Generative topographic mapping for seismic facies estimation of a carbonate wash, Veracruz Basin, southern Mexico: Interpretation, **2**, SA31–SA47, doi: 10.1190/INT-2013-0077.1.

Sheffield, T. M., and B. A. Parne, 2008, Geovolume visualization and interpretation: What makes a useful visualization seismic attribute?: 78th Annual International Meeting, SEG, Expanded Abstracts, 849–853.

Shi, J., and J. Malik, 2000, Normalized cuts and image segmentation: IEEE Transactions on Pattern Analysis and Machine Intelligence, **22**, 838–905.

Wallet, B., and R. E. F. Pepper, 2013, Using mathematical morphology in an attribute workflow to improve the interpretability of salt bodies in the Gulf of Mexico: 83rd Annual International Meeting, SEG, Expanded Abstracts, 1324–1328.

West, P. B., R. S. May, E. J. Eastwood, and C. Rossen, 2002, Interactive seismic facies classification using textural attributes and neural networks: The Leading Edge, **21**, 1042–1049, doi: 10.1190/1.1518444.

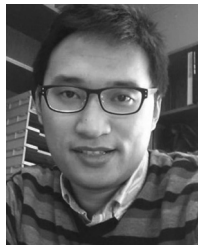

Jie Qi received a B.S. from the China University of petroleum, Beijing, China, and an M.S. from the University of Houston. He is a Ph.D. student of geophysics and also a research assistant at the University of Oklahoma, Norman. In 2011, he studied at the University of Houston and also worked as a research assistant in spectral decomposition and seismic interpretation. He is a member of SEG, AAPG, and the Geophysical Society of Houston. His research interests include pattern recognition, seismic attribute interpretation, seismic inversion, and seismic facies analysis.

Kurt J. Marfurt joined the University of Oklahoma (OU) in 2007, where he serves as the Frank and Henrietta Schultz Professor of Geophysics within the ConocoPhillips School of Geology and Geophysics. His recent work has been focused on correlating seismic attributes, such as volumetric curvature, impedance inversion, and azimuthal anisotropy with image logs and microseismic measurements with a particular focus on resource plays. In addition to teaching and research duties at OU, he leads short courses on attributes for SEG and AAPG. His primary research interests include development and calibration of new seismic attributes to aid in seismic processing, seismic interpretation, and reservoir characterization.

Biographies and photographs of the other authors are not available.